


Warping caused by surface elasticity in a nanowire under torsion

Jean-Marc Roussel¹* and Marc Gailhanou¹

Aix Marseille Université, CNRS, IM2NP UMR 7334, 13397 Marseille, France

 (Received 5 October 2022; revised 28 February 2023; accepted 2 March 2023; published 21 March 2023)

By combining molecular statics simulations and continuum mechanics-based modeling, we show in this paper that the torsion of a (001) single-crystal copper nanowire with a circular cross section gives rise to a warp, i.e., to a displacement field along the wire axis that renders the cross section nonplanar. This behavior, which is in apparent contradiction with what is predicted by continuum mechanics for an isotropic cylinder, can be well explained if we take into account the elastic response of the wire lateral surface. The latter is characterized by the anisotropy of the surface elastic constants and, more specifically in the case of torsion, by the surface shear constant C_{44}^S whose strength as a function of the local orientation of the lateral surface is estimated independently from atomistic calculations on slabs presenting different vicinal surfaces. The solution of the torsion problem is then obtained by adopting a semi-inverse method in the framework of the finite strain theory in linear elasticity with Gurtin-Murdoch boundary conditions linking surface stress and bulk stress. It is shown that such an approach is well suited to explain quantitatively the warp obtained in our atomistic simulations and to prove the preponderant role played by the surface elastic constant C_{44}^S .

DOI: [10.1103/PhysRevB.107.094110](https://doi.org/10.1103/PhysRevB.107.094110)

I. INTRODUCTION

The issue of the mechanical behavior of a nanowire has led to numerous research works [1,2], both experimental and theoretical, where the atomistic simulations have also played a key role in the understanding of the phenomena [3,4]. A nanowire differs from a macroscopic wire by two main characteristics that could be summarized as follows. (i) First, it is a cylindrical nano-object made usually of a single crystal. Consequently, one can expect anisotropic mechanical behaviors for metal nanowires depending on the crystallographic orientation of the wire. (ii) Second, it is an object which has a large surface area to volume ratio in number of atoms. This great proximity of the lateral surface also affects the nanowire mechanics. Close to the surface, the elastic response is very different from that of the volume. And regarding the plasticity, the surface is also the place where dislocations can nucleate or conversely escape the wire.

In single-crystal nanowires plasticity mechanisms depend on the orientation of the wires. This has been clearly shown in the molecular dynamics work of Weinberger and Cai where the plastic response of single-crystal metal nanowires subject to uniaxial loading, torsion, or bending have been studied extensively [5]. A particularly interesting case discussed by these authors is that of Au (110) nanowire subjected to torsion. Under strong torsion, partial dislocations parallel to the nanowire axis are nucleated. However, these partials remain unstable in the absence of the applied torque. This leads the authors to invoke a pseudoelastic behavior for Au (110) nanowire since when it is unloaded, the partials escape the wire and the twist angle returns to zero [5].

Another feature of nanowires is that the stability of the crystal defects is modified by the proximity of the lateral

surfaces. Let us take the example of a screw dislocation lying at the center of a macroscopic wire of circular cross section. The Eshelby solution predicts that its stability is independent of the wire radius [6]. This is no longer true in a nanowire because the size of the core of the screw dislocation, which dissociates into two partials in many metals, is no longer negligible compared to the diameter of the nanowire. This leads to a lowering of the Eshelby barrier when the radius of the nanowire decreases and thus to a decrease of the stability of the dislocation [7].

Surface stress and surface elastic constants can also play a role on the effective elastic moduli of nanowires as recently discussed by Elsner *et al.* [8]. More specifically, in the case of the torsion of nanowire, these authors show that the torsional rigidity depends also on the surface shear elastic constant (we will denote C_{44}^S). According to this theoretical study, the relative change in effective stiffness due to the surface elastic constant C_{44}^S will be more and more pronounced for small diameter nanowires. However, in this analysis proposed by Elsner *et al.* [8], an important physical aspect which is present for any nanowire was not addressed: the fact that the surface shear constant C_{44}^S (denoted by \mathbb{C}_{44} in Ref. [8]) varies inevitably with the azimuth Θ , i.e., with the local orientation of the lateral surface. On the one hand, this anisotropic property of the surface does not really change the expression of the torsional stiffness since ultimately only an estimate of the average value of C_{44}^S over the entire lateral surface of the wire can be used. But, on the other hand, we will show in this work that this anisotropic property of the surface should not be neglected if one wishes to describe the deformation state of a nanowire under torsion.

The purpose of this study is therefore to show how the anisotropy of the surface elastic constant C_{44}^S produces a deformation field in the nanowire under torsion. We will see that the bulk stress induced by the surface stress leads to a warping of the nanowire under torsion, i.e., the fact that the

*Corresponding author: jean-marc.roussel@univ-amu.fr

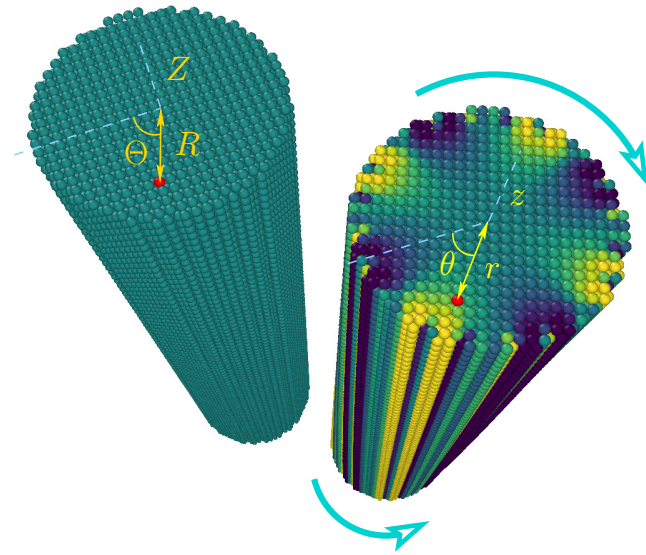


FIG. 1. Illustration of the torsion problem addressed in this work. A copper $\langle 001 \rangle$ nanowire of circular cross section is subjected to a twisting moment at its ends. The torsion gives rise to a displacement of the atomic columns along the wire axis (represented by the color scale) and therefore to a warping of the nanowire. In the undeformed wire (on the left), an atom found at the position (R, Θ, Z) in cylindrical coordinates occupies the position (r, θ, z) in the twisted wire (on the right).

cross section does not remain plane under torsion as illustrated in Fig. 1. The warp induced by torsion is often encountered in mechanics [9]. These nonuniform out-of-plane displacements will appear for instance if the cross section is not circular and/or if the bulk shear modulus in the plane of the cross section is anisotropic. We will show in this work that surface elasticity is also the cause of a warp. To explore this behavior, we consider the torsion of a single-crystal $\langle 001 \rangle$ copper wire of circular cross section for which warping in principle does not occur.

The demonstration of this warping will be done both numerically by molecular statics simulations and analytically by solving the torsion problem. The second approach requires to apply the so-called generalized Young-Laplace conditions [10] which link at the surface the components of the surface stress tensor to some components of the bulk stress tensor. These relations of local equilibrium established by Gurtin and Murdoch [11] are detailed in Sec. II A as well as the mathematical modeling of the torsion we are proposing in the framework of the finite strain theory and linear elasticity. Finite strain theory is necessary to address the large rotations observed along the wire under torsion while linear elasticity is sufficient to describe the small deformations studied in this work [12]. In Sec. III, we present some important aspects of the atomistic calculations performed using the SMA (tight binding second moment approximation) potential [13,14]. We describe in particular how atomic strain and stress tensors can be calculated. We also detail how are determined the relevant physical quantities involved in the continuum model, namely, the bulk elastic constants and the surface excess elastic parameters. For the latter, additional atomistic calculations on deformed slabs with vicinal surfaces were performed to

evaluate the anisotropy of the surface elastic constants. Finally, in Sec. IV, evidences of the warping in nanowires under torsion are given from our atomistic simulations. We show that this displacement field observed in the simulations is in very good agreement with the explicit solution obtained from our continuum mechanics-based modeling where the anisotropy of the elastic surface shear constant C_{44}^S is taken into account.

II. CONTINUUM MODEL

A. Torsion of a circular cylinder of Cu

In this section we present our continuum model based on finite strain theory and linear elasticity. By adopting a semi-inverse approach, we first propose a model deformation map which reproduces the torsion and is likely to generate a warp. From this map, we derive the bulk and surface strain tensors. Then the equilibrium equations are established in terms of the first Piola-Kirchhoff stress tensor (PK1) in the volume and at the surface according to the theory of Gurtin and Murdoch. Finally, the stress-strain relations are detailed to obtain the PK1 stress involved in the equilibrium equations.

The problem of concern here is that of a very long solid circular cylinder of radius R_0 composed of crystalline face-centered-cubic (fcc) copper subjected to a twisting moment at its ends. The main axis of the wire is oriented along a $\langle 001 \rangle$ direction. The undeformed configuration is chosen to be the state where all atoms occupy initially the bulk crystal lattice. The current configuration is then the result of two successive deformations. First, the free wire is relaxed to its equilibrium state without torsion. The surface atoms being in tension in metals, the relaxation is a contraction of the wire along its long dimension with a radial deformation. Then, the relaxed wire is subjected to a twisting moment at its ends. To model these two successive deformations, one has to describe the deformation map φ as

$$\mathbf{x} = \varphi(\mathbf{X}) \quad (1)$$

which relates the position vectors \mathbf{X} of the atoms in the reference (undeformed) configuration to their position vectors \mathbf{x} in the current configuration. On using cylindrical coordinates (R, Θ, Z) in the undeformed configuration and (r, θ, z) in the current configuration, we may model the current configuration as follows:

$$r = (1 + u_0)R, \quad \theta = \Theta + \alpha Z, \quad z = \alpha R_0 g(R, \Theta) + (1 + w_0)Z \quad (2)$$

or using a matrix representation

$$\begin{pmatrix} r \\ \theta \\ z \end{pmatrix} = \begin{pmatrix} 1 + u_0 & 0 & 0 \\ 0 & 1 & \alpha \\ \alpha R_0 g/R & 0 & 1 + w_0 \end{pmatrix} \begin{pmatrix} R \\ \Theta \\ Z \end{pmatrix}, \quad (3)$$

where α denotes the twist per unit undeformed length, R_0 is the radius of the wire, u_0 and w_0 set the relaxed state before torsion, and $u_z^w = \alpha R_0 g(R, \Theta)$ is the warp displacement field to be determined. Its form proportional to α is similar to the one generally encountered if the wire direction is anisotropic (e.g., $[011]$ for Cu) or if the cross section is noncircular [15]. We will show in this work that our model in Eq. (2) is well suited to explain the warp induced by the surface excess

elasticity. It is worth noting, however, that this model cannot describe the radial deformation and the change in length of the wire caused by the torsion. To be reproduced, these nonlinear effects (called Poynting effects) require additional $(\alpha R_0)^2$ terms in Eq. (2) which are not considered in this work [16]. Besides, even without torsion for $\alpha = 0$, it is assumed in our model that the radial deformation (described only by u_0) at equilibrium is constant. This is clearly a simplified description of the in-plane displacement fields which has to be refined, for instance, by considering and extending the recent work of Wang *et al.* [17] which establishes for isotropic solid cylinders (our case is anisotropic), some analytic expressions of the in-plane displacements in terms of series expansions. In this work, however, since the warp we wish to explain is not correlated to these in-plane displacements, the simplified description of these latter in terms of u_0 will be kept for clarity.

To relate an infinitesimal line element $d\mathbf{X}$ in the undeformed configuration to its spatial counterpart $d\mathbf{x}$ in the current configuration, one defines the deformation gradient tensor field \mathbf{F} such as

$$d\mathbf{x} = \mathbf{F}d\mathbf{X}, \quad (4)$$

where $\mathbf{F} = \text{Grad}\varphi$. For the mapping considered in Eq. (2), the resulting deformation gradient can be written as

$$\begin{aligned} \mathbf{F} = & (1 + u_0)(\mathbf{e}_r \otimes \mathbf{e}_R + \mathbf{e}_\theta \otimes \mathbf{e}_\Theta + \alpha R \mathbf{e}_\theta \otimes \mathbf{e}_Z) \\ & + \alpha R_0(g'_R \mathbf{e}_z \otimes \mathbf{e}_R + g'_\Theta/R \mathbf{e}_z \otimes \mathbf{e}_\Theta) \\ & + (1 + w_0)\mathbf{e}_z \otimes \mathbf{e}_Z, \end{aligned} \quad (5)$$

where $(\mathbf{e}_R, \mathbf{e}_\Theta, \mathbf{e}_Z)$ and $(\mathbf{e}_r, \mathbf{e}_\theta, \mathbf{e}_z)$ are the cylindrical basis in the reference and deformed state, respectively. Using a matrix representation

$$\mathbf{F} = \begin{pmatrix} 1 + u_0 & 0 & 0 \\ 0 & 1 + u_0 & (1 + u_0)\alpha R \\ \alpha R_0 g'_R & \alpha R_0 g'_\Theta/R & 1 + w_0 \end{pmatrix}, \quad (6)$$

where $g'_R = \partial g/\partial R$ and $g'_\Theta = \partial g/\partial \Theta$.

To measure the deformation, we use the finite strain tensor \mathbf{E} (also called Lagrangian or Green's strain tensor) defined as [12,18] $\mathbf{E} = \frac{1}{2}(\mathbf{F}^T \mathbf{F} - \mathbf{I})$ where \mathbf{I} is the unit tensor. Considering that $u_0 \ll 1$ and $w_0 \ll 1$ and neglecting second-order [including $(\alpha R_0)^2$] terms, \mathbf{E} can be written as

$$\begin{aligned} \mathbf{E} = & u_0(\mathbf{e}_R \otimes \mathbf{e}_R + \mathbf{e}_\Theta \otimes \mathbf{e}_\Theta) + w_0 \mathbf{e}_Z \otimes \mathbf{e}_Z \\ & + \alpha R_0[(R/R_0 + g'_\Theta/R)(\mathbf{e}_\Theta \otimes \mathbf{e}_Z + \mathbf{e}_Z \otimes \mathbf{e}_\Theta) \\ & + g'_R(\mathbf{e}_R \otimes \mathbf{e}_Z + \mathbf{e}_Z \otimes \mathbf{e}_R)]/2 \end{aligned} \quad (7)$$

or using a matrix representation

$$\begin{aligned} \mathbf{E} = & \begin{pmatrix} u_0 & 0 & 0 \\ 0 & u_0 & 0 \\ 0 & 0 & w_0 \end{pmatrix} \\ & + \frac{\alpha R_0}{2} \begin{pmatrix} 0 & 0 & g'_R \\ 0 & 0 & R/R_0 + g'_\Theta/R \\ g'_R & R/R_0 + g'_\Theta/R & 0 \end{pmatrix}. \end{aligned} \quad (8)$$

To account for the difference in elastic behavior on the surface and inside the bulk we employ the Gurtin-Murdoch theory [11]. In this framework, one can define a surface deformation gradient, denoted \mathbf{F}^S , which relates an infinitesimal

line element $d\mathbf{X}$ tangent to the undeformed surface \mathcal{S}_0 to its spatial counterpart $d\mathbf{x}$ tangent to the current surface via the relation $d\mathbf{x} = \mathbf{F}^S d\mathbf{X}$.

Defining the surface deformation map φ^S as equal to $\varphi(X \in \mathcal{S}_0)$ in Eq. (1), \mathbf{F}^S is determined from $\mathbf{F}^S = \text{Grad}^S \varphi^S$ where $\text{Grad}^S\{\cdot\} = \text{Grad}\{\cdot\} \cdot \mathbf{I}^S$ and where $\mathbf{I}^S = \mathbf{I} - \mathbf{e}_R \otimes \mathbf{e}_R$ denotes the surface unit tensor at any point of the lateral surface of the initial circular cylinder [19]. In practice, the matrix representation of \mathbf{F}^S can therefore be obtained directly from \mathbf{F} in Eq. (6) by canceling the three components of the first column and by replacing R by R_0 in the six other components which in the general case can be different from zero. In the present case, we have

$$\mathbf{F}^S = \begin{pmatrix} 0 & 0 & 0 \\ 0 & 1 + u_0 & (1 + u_0)\alpha R_0 \\ 0 & \alpha g'_\Theta(R_0) & 1 + w_0 \end{pmatrix}. \quad (9)$$

Finally for a circular nanowire, the symmetrical strain \mathbf{E}^S on the surface is described by three independent components only. \mathbf{E}^S can be obtained either from the expression of \mathbf{F}^S in Eq. (9) using the definition $\mathbf{E}^S = \frac{1}{2}(\mathbf{F}^{S^T} \mathbf{F}^S - \mathbf{I}^S)$ or equivalently from \mathbf{E} in Eq. (8) using the derived relation $\mathbf{E}^S = \mathbf{I}^S \mathbf{E} \mathbf{I}^S$ which leads in our case to

$$\begin{aligned} \mathbf{E}^S = & u_0 \mathbf{e}_\Theta \otimes \mathbf{e}_\Theta + w_0 \mathbf{e}_Z \otimes \mathbf{e}_Z \\ & + \alpha R_0[1 + g'_\Theta(R_0)/R_0] \\ & \times (\mathbf{e}_\Theta \otimes \mathbf{e}_Z + \mathbf{e}_Z \otimes \mathbf{e}_\Theta)/2, \end{aligned} \quad (10)$$

where $g'_\Theta(R_0)$ is evaluated at $R = R_0$. Using a matrix representation, we have

$$\mathbf{E}^S = \begin{pmatrix} u_0 & 0 \\ 0 & w_0 \end{pmatrix} + \frac{\alpha R_0}{2} \begin{pmatrix} 0 & 1 + g'_\Theta(R_0)/R_0 \\ 1 + g'_\Theta(R_0)/R_0 & 0 \end{pmatrix}. \quad (11)$$

Let us now introduce the so-called Piola-Kirchhoff stress tensors which appear in the material (Lagrangian) description. Assuming that the bulk strain energy $\psi(\mathbf{E})$ per unit undeformed volume and the surface strain energy $\psi^S(\mathbf{E}^S)$ per unit undeformed area are known, the *second* Piola-Kirchhoff stress tensors are defined as $\mathbf{S} = d\psi/d\mathbf{E}$ in the bulk and $\mathbf{S}^S = d\psi^S/d\mathbf{E}^S$ at the surface.

Moreover, the *first* Piola-Kirchhoff stress tensor \mathbf{P} which will be used to formulate the equilibrium conditions is deduced in the bulk from the product $\mathbf{P} = \mathbf{F}\mathbf{S}$. Similarly at the surface, this stress tensor becomes $\mathbf{P}^S = \mathbf{F}^S \mathbf{S}^S$.

Finally, to recover the usual Cauchy stress tensor $\boldsymbol{\sigma}$ which is adequate in the spatial (Eulerian) description, the relation $\boldsymbol{\sigma} = J^{-1} \mathbf{F} \mathbf{P}$ can be used with $J = \det(\mathbf{F})$ being the determinant of \mathbf{F} .

In absence of body force, the equilibrium condition formulated with the first Piola-Kirchhoff stress tensor \mathbf{P} reads as [12,18]

$$\text{Div} \mathbf{P} = \frac{\partial \mathbf{P}}{\partial R} \mathbf{e}_R + \frac{1}{R} \frac{\partial \mathbf{P}}{\partial \Theta} \mathbf{e}_\Theta + \frac{\partial \mathbf{P}}{\partial Z} \mathbf{e}_Z = \mathbf{0}, \quad (12)$$

where Div is the divergence operator in cylindrical coordinates. The two-point tensor \mathbf{P} can be written in terms of its

components as

$$\begin{aligned} \mathbf{P} = & P_{rR} \mathbf{e}_r \otimes \mathbf{e}_R + P_{r\Theta} \mathbf{e}_r \otimes \mathbf{e}_\Theta + P_{rZ} \mathbf{e}_r \otimes \mathbf{e}_Z \\ & + P_{\theta R} \mathbf{e}_\theta \otimes \mathbf{e}_R + P_{\theta\Theta} \mathbf{e}_\theta \otimes \mathbf{e}_\Theta + P_{\theta Z} \mathbf{e}_\theta \otimes \mathbf{e}_Z \\ & + P_{zR} \mathbf{e}_z \otimes \mathbf{e}_R + P_{z\Theta} \mathbf{e}_z \otimes \mathbf{e}_\Theta + P_{zZ} \mathbf{e}_z \otimes \mathbf{e}_Z. \end{aligned} \quad (13)$$

Equation (12) yields a system of three scalar equations involving these nine components as follows [20]:

$$\begin{aligned} \frac{\partial P_{rR}}{\partial R} + \frac{1}{R} \frac{\partial P_{r\Theta}}{\partial \Theta} + \frac{P_{rR}}{R} - \frac{P_{\theta\Theta}}{R} \frac{\partial \theta}{\partial \Theta} + \frac{\partial P_{rZ}}{\partial Z} \\ - P_{\theta R} \frac{\partial \theta}{\partial R} - P_{\theta Z} \frac{\partial \theta}{\partial Z} = 0, \\ \frac{\partial P_{\theta R}}{\partial R} + \frac{1}{R} \frac{\partial P_{\theta\Theta}}{\partial \Theta} + \frac{P_{\theta R}}{R} + \frac{P_{r\Theta}}{R} \frac{\partial \theta}{\partial \Theta} + \frac{\partial P_{\theta Z}}{\partial Z} \\ + P_{rR} \frac{\partial \theta}{\partial R} + P_{rZ} \frac{\partial \theta}{\partial Z} = 0, \\ \frac{\partial P_{zR}}{\partial R} + \frac{1}{R} \frac{\partial P_{z\Theta}}{\partial \Theta} + \frac{P_{zR}}{R} + \frac{\partial P_{zZ}}{\partial Z} = 0. \end{aligned} \quad (14)$$

At the lateral surface of the circular nanowire, the local equilibrium in absence of external load obeys the Gurtin-Murdoch condition [11,21] (also called generalized Young-Laplace conditions [10])

$$\mathbf{P} \mathbf{e}_R - \text{Div}^S \mathbf{P}^S = \mathbf{0}. \quad (15)$$

Here, $\text{Div}^S \mathbf{P}^S$ is the surface divergence of the superficial tensor field \mathbf{P}^S (for details on differential geometry of surfaces, see for instance Steinmann *et al.* [22] and the references therein). It is defined as $\text{Div}^S \mathbf{P}^S = \frac{\partial \mathbf{P}^S}{\partial \alpha^1} \mathbf{s}^1 + \frac{\partial \mathbf{P}^S}{\partial \alpha^2} \mathbf{s}^2$ where α^1, α^2 are the surface coordinates and $\mathbf{s}^1, \mathbf{s}^2$ are the contravariant basis vectors in the tangent plane of S_0 [20]. Since in our case, S_0 is the surface of the undeformed cylinder, we simply have $\alpha^1 = \Theta, \alpha^2 = Z, \mathbf{s}^1 = \mathbf{e}_\Theta/R_0$, and $\mathbf{s}^2 = \mathbf{e}_Z$ leading to

$$\text{Div}^S \mathbf{P}^S = \frac{1}{R_0} \frac{\partial \mathbf{P}^S}{\partial \Theta} \mathbf{e}_\Theta + \frac{\partial \mathbf{P}^S}{\partial Z} \mathbf{e}_Z. \quad (16)$$

In terms of the components of \mathbf{P} and \mathbf{P}^S , the generalized Young-Laplace conditions can be written as

$$\begin{aligned} P_{rR}|_{R=R_0} &= \frac{1}{R_0} \frac{\partial P_{r\Theta}^S}{\partial \Theta} - \frac{P_{\theta\Theta}^S}{R_0} \frac{\partial \theta}{\partial \Theta} + \frac{\partial P_{rZ}^S}{\partial Z} - P_{\theta Z}^S \frac{\partial \theta}{\partial Z}, \\ P_{\theta R}|_{R=R_0} &= \frac{1}{R_0} \frac{\partial P_{\theta\Theta}^S}{\partial \Theta} + \frac{P_{r\Theta}^S}{R_0} \frac{\partial \theta}{\partial \Theta} + \frac{\partial P_{\theta Z}^S}{\partial Z} + P_{rZ}^S \frac{\partial \theta}{\partial Z}, \\ P_{zR}|_{R=R_0} &= \frac{1}{R_0} \frac{\partial P_{z\Theta}^S}{\partial \Theta} + \frac{\partial P_{zZ}^S}{\partial Z}. \end{aligned} \quad (17)$$

Finally, to account for the fact that the nanowire is very long and free to relax along its main axis (no end effects), the integral equilibrium condition on a cross section S of normal vector \mathbf{e}_Z and its circular boundary ∂S reads as (far from the wire extremities)

$$\iint_S P_{zZ} dA + \int_{\partial S} P_{zZ}^S dL = 0, \quad (18)$$

where dA is the area element on S and dL the line element on ∂S in the material configuration. The interpretation of Eq. (18) is simple: consider the two parts of the wire separated by the cross section S , the net force normal to S exerted by one part on the other is null at equilibrium as illustrated in Fig. 10 of the Appendix.

To demonstrate the presence of a warp induced by surface elasticity, we will show that it is not necessary to invoke nonlinear phenomena due to large strain. Indeed, the warp may be observed in conditions of low strain; however, since the nanowire is subjected to torsion, large rotations will inevitably appear in the nanowire. This is the reason why the linear elasticity theory is used with a description of the strain given by the tensors \mathbf{E} and \mathbf{E}^S which are not affected by large rotations. In this framework, the bulk energy density $\psi(\mathbf{E})$ depends only on the second-order elastic constants C_{ij} where i and j range over the values 1, 2, ..., 6 in the Voigt's convention. By accounting for the symmetry $C_{ij} = C_{ji}$, strain changes the six components S_i of the symmetric bulk stress \mathbf{S} according to

$$S_i = C_{ij} E_j \quad (19)$$

using Einstein summation convention and Brugger notation [23] to identify the components in curvilinear coordinates: $S_1 = S_{RR}, S_2 = S_{\Theta\Theta}, S_3 = S_{ZZ}, S_4 = S_{\Theta Z}, S_5 = S_{RZ}, S_6 = S_{R\Theta}$, and $E_1 = E_{RR}, E_2 = E_{\Theta\Theta}, E_3 = E_{ZZ}, E_4 = 2E_{\Theta Z}, E_5 = 2E_{RZ}, E_6 = 2E_{R\Theta}$.

In a reference frame rotating with the angle Θ around a $\langle 001 \rangle$ direction, only the following constants are not null: $C_{11}, C_{12}, C_{13}, C_{16}, C_{22}, C_{23}, C_{26}, C_{33}, C_{44}, C_{55}$, and C_{66} . Besides, it is worth noting that some C_{ij} depend on the azimuth Θ as illustrated in Fig. 3. For $\langle 001 \rangle$ wires considered here, this anisotropic behavior of C_{ij} presents a fourfold symmetry and appears if the subscripts i and j are equal to 1, 2, or 6. Applying the linear relation of Eq. (19) to the expression of \mathbf{E} given by Eq. (7), we obtain in the bulk

$$\begin{aligned} S_{RR} &= C_{11} E_{RR} + C_{12} E_{\Theta\Theta} + C_{13} E_{ZZ}, \\ S_{\Theta\Theta} &= C_{12} E_{RR} + C_{22} E_{\Theta\Theta} + C_{23} E_{ZZ}, \\ S_{ZZ} &= C_{13} E_{RR} + C_{23} E_{\Theta\Theta} + C_{33} E_{ZZ}, \\ S_{\Theta Z} &= 2C_{44} E_{\Theta Z}, \\ S_{RZ} &= 2C_{55} E_{RZ}, \\ S_{R\Theta} &= 0. \end{aligned} \quad (20)$$

Considering again that $u_0 \ll 1$ and $w_0 \ll 1$ and neglecting $(\alpha R_0)^2$ terms, the *first* Piola-Kirchhoff stress tensor \mathbf{P} can be written using a matrix representation as

$$\mathbf{P} = \begin{pmatrix} S_{RR} & 0 & S_{RZ} \\ 0 & S_{\Theta\Theta} & S_{\Theta Z} + F_{\theta Z} S_{ZZ} \\ S_{RZ} + F_{zR} S_{RR} & S_{\Theta Z} + F_{z\Theta} S_{\Theta\Theta} & S_{ZZ} \end{pmatrix}, \quad (21)$$

where according to Eq. (5), we have $F_{\theta Z} = \alpha R, F_{zR} = \alpha R_0 g'_R$, and $F_{z\Theta} = \alpha R_0 g'_\Theta / R$.

Similarly at the surface, the linear elasticity theory allows us to write the three components $S_{\Theta\Theta}^S, S_{\Theta Z}^S$, and S_{ZZ}^S of the

surface stress tensor \mathbf{S}^S as follows:

$$\begin{aligned} S_{\Theta\Theta}^S &= S_{\Theta\Theta}^{S,0} + C_{22}^S E_{\Theta\Theta}^S + C_{23}^S E_{ZZ}^S, \\ S_{ZZ}^S &= S_{ZZ}^{S,0} + C_{23}^S E_{\Theta\Theta}^S + C_{33}^S E_{ZZ}^S, \\ S_{\Theta Z}^S &= 2C_{44}^S E_{\Theta Z}^S, \end{aligned} \quad (22)$$

where $S_{\Theta\Theta}^{S,0}$ and $S_{ZZ}^{S,0}$ are the two surface stress components at $\mathbf{E}^S = \mathbf{0}$ and C_{22}^S , C_{23}^S , C_{33}^S , and C_{44}^S the four surface elastic constants required to determine the linear elastic response of the nanowire. It is worth noting that these parameters depend in theory on the local orientation of the lateral surface of the wire (i.e., on the azimuth Θ). To clarify this anisotropic property, let us take the case of the $\langle 001 \rangle$ circular wire considered in this work. For $\Theta = 0$, the lateral surface resembles a $\{100\}$ surface, but for $\Theta = \pi/4$ it is the atomic structure of the $\{110\}$ surface which is observed, and for any other value of Θ , the local morphology of the surface will approach that of a vicinal surface. Since the atomic structure and symmetry of the $\{100\}$ and the $\{110\}$ surfaces are very different, one can also expect different values of the surface elastic parameters in Eq. (22). For instance, an immediate consequence of the change in symmetry is the fact that $S_{\Theta\Theta}^{S,0}$ and $S_{ZZ}^{S,0}$ differ for the $\{110\}$ surface, while they are equal for the $\{100\}$ surface [24]. But, more importantly in this study focused on the torsion, the surface shear elastic constant C_{44}^S in Eq. (22) is a key parameter that also varies continuously with Θ . This anisotropic behavior of C_{44}^S (denoted by \mathbb{C}_{44} in Ref. [8]) is generally not taken into account. We will show, however, that it has interesting implications since it is responsible of a warp in the bulk of the wire via the Gurtin-Murdoch condition of Eq. (15). For this purpose, we also need to write the *first* Piola-Kirchhoff surface stress $\mathbf{P}^S = \mathbf{F}^S \mathbf{S}^S$. The form of \mathbf{F}^S in Eq. (9) implies that $P_{r\Theta}^S$ and P_{rZ}^S are null, and the four remaining components appear in \mathbf{P}^S as follows:

$$\mathbf{P}^S = \begin{pmatrix} 0 & 0 & 0 \\ 0 & S_{\Theta\Theta}^S & S_{\Theta Z}^S + F_{\Theta Z}^S S_{ZZ}^S \\ 0 & S_{\Theta Z}^S + F_{z\Theta}^S S_{\Theta\Theta}^S & S_{ZZ}^S \end{pmatrix}, \quad (23)$$

where $F_{\Theta Z}^S = \alpha R_0$ and $F_{z\Theta}^S = \alpha g'_{\Theta}(R_0)$.

B. Relaxed state before torsion: u_0, w_0

Let us first consider the free untwisted circular nanowire whose equilibrium state is fixed by the parameters u_0 and w_0 introduced in Eq. (2). For $\alpha = 0$, the stress \mathbf{P} expressed in Eq. (21) is reduced to

$$\mathbf{P} = \begin{pmatrix} S_{RR} & 0 & 0 \\ 0 & S_{\Theta\Theta} & 0 \\ 0 & 0 & S_{ZZ} \end{pmatrix}, \quad (24)$$

where using the bulk elastic constants C_{ij} in cylindrical coordinates given in Fig. 3 of Sec. III A for the $\langle 001 \rangle$ fcc wire and their relations with the usual three elastic constants C_{11}^0 , C_{12}^0 , and C_{44}^0 defined for a cubic crystal, we have

$$\begin{aligned} S_{RR} &= (C_{11} + C_{12})u_0 + C_{13}w_0 = (C_{11}^0 + C_{12}^0)u_0 + C_{12}^0 w_0, \\ S_{\Theta\Theta} &= (C_{21} + C_{22})u_0 + C_{23}w_0 = (C_{11}^0 + C_{12}^0)u_0 + C_{12}^0 w_0, \\ S_{ZZ} &= (C_{31} + C_{32})u_0 + C_{33}w_0 = 2C_{12}^0 u_0 + C_{11}^0 w_0. \end{aligned} \quad (25)$$

As mentioned above, the parameter u_0 in Eq. (2) is considered constant and should be seen as the first term of a (R, Θ) series expansion. In this simplified case, S_{RR} , $S_{\Theta\Theta}$, and S_{ZZ} in Eq. (25) become also independent of R and Θ . The resulting stress \mathbf{P} in Eq. (24) is therefore solution of the bulk equilibrium equation (12) and its components are only determined by the conditions given in Eqs. (17) and (18). These latter relate the bulk stress \mathbf{P} to the surface stress \mathbf{P}^S [Eq. (23)] as follows:

$$\begin{aligned} S_{RR}|_{R=R_0} &= -\frac{S_{\Theta\Theta}^S}{R_0}, \\ \int_0^{2\pi} \int_0^{R_0} S_{ZZ} R dR d\Theta + R_0 \int_0^{2\pi} S_{ZZ}^S d\Theta &= 0. \end{aligned} \quad (26)$$

The first relation in Eq. (26) is local and depends on Θ ; however, to be consistent with the fact that u_0 is constant, we will use average values of the surface excess elastic parameters which control $S_{\Theta\Theta}^S$ in Eq. (22). Thus, considering Eqs. (22), (25), and (26), we obtain the couple (u_0, w_0) from the following simple system of equations:

$$\begin{aligned} \left(C_{11}^0 + C_{12}^0 + \frac{\overline{C_{22}^S}}{R_0} \right) u_0 + \left(C_{12}^0 + \frac{\overline{C_{23}^S}}{R_0} \right) w_0 &= -\frac{\overline{S_{\Theta\Theta}^{S,0}}}{R_0}, \\ \left(2C_{12}^0 + 2\frac{\overline{C_{23}^S}}{R_0} \right) u_0 + \left(C_{11}^0 + 2\frac{\overline{C_{33}^S}}{R_0} \right) w_0 &= -2\frac{\overline{S_{ZZ}^{S,0}}}{R_0}, \end{aligned} \quad (27)$$

where $\overline{C_{ij}^S}$, $\overline{S_{\Theta\Theta}^{S,0}}$, and $\overline{S_{ZZ}^{S,0}}$ are average values over Θ such as $\overline{C_{ij}^S} = \frac{1}{2\pi} \int_0^{2\pi} C_{ij}^S d\Theta$. This integral depends on the orientation of the wire which is $\langle 001 \rangle$ here. Its value requires atomistic calculations of the surface elastic parameters as a function of Θ which are presented in Sec. III B. In Fig. 2, we compare the values of u_0 and w_0 obtained from Eqs. (27) to the ones calculated from our molecular statics simulations. We note that both approaches give close values of u_0 and w_0 for various wire radii R_0 ranging from 2.5 to 30 nm. For large R_0 where $u_0/w_0 \approx (1/2 - C_{12}^0/C_{11}^0)$ from Eqs. (27) considering $\overline{S_{\Theta\Theta}^{S,0}} \approx \overline{S_{ZZ}^{S,0}}$, the axial contraction of the wire w_0 and the average radial expansion u_0 are proportional to $1/R_0$, but they deviate from this law for small radii. This behavior shown in Fig. 2 is well reproduced and explained by the model given in Eqs. (27). Clearly, the deviation from the $1/R_0$ law is due to the parameters $\overline{C_{ij}^S}$ whose influence increases for small values of R_0 .

C. Warp function under torsion: $g(R, \Theta)$

Let us now consider the free circular Cu nanowire twisted by an angle α . On the bulk side, the stress tensor \mathbf{P} expressed in Eq. (21) must fulfill the equilibrium equations (14). The two first equations involve only $(\alpha R_0)^2$ terms and are neglected but from the third equilibrium equation, using Eqs. (8), (20), and (21), we obtain that the warp function $g(R, \Theta)$ should be solution of the following differential equation:

$$(C_{55} + S_{RR}) \left(g''_R + \frac{g'_R}{R} \right) + (C_{44} + S_{\Theta\Theta}) \frac{g''_{\Theta}}{R^2} = 0, \quad (28)$$

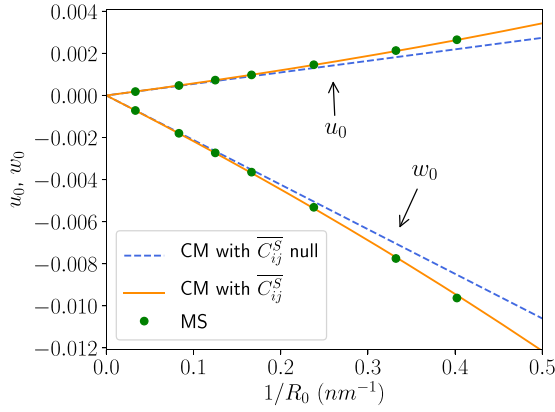


FIG. 2. Influence of the surface elastic constants C_{ij}^S on the axial contraction w_0 and the radial expansion u_0 in $\langle 001 \rangle$ Cu nanowire of circular cross section (before torsion) given by Eqs. (27) resulting from the continuum model (CM). The elastic constants are calculated in Sec. III B: $C_{11}^0 = 169$ GPa and $C_{12}^0 = 127$ GPa, $S_{\Theta\Theta}^{S,0} = 1.071$ J m $^{-2}$, $S_{ZZ}^{S,0} = 1.096$ J m $^{-2}$, $C_{22}^S = -4.88$ J m $^{-2}$, $C_{23}^S = -0.02$ J m $^{-2}$, and $C_{33}^S = -7.05$ J m $^{-2}$. The CM curves are compared to the results of molecular statics simulations (MS) performed on various $\langle 001 \rangle$ Cu nanowires. The MS value of the radial expansion u_0 is calculated by averaging the radial displacement u_R of atoms located at a distance $R_0/2$ from the center so that $u_0 = \frac{1}{\pi R_0} \int_0^{2\pi} u_R d\Theta$.

where $g'_R = \partial g'_R / \partial R$ and $g'_\Theta = \partial g'_R / \partial \Theta$. Noting from Eqs. (8) and (20) that $S_{RR} = S_{\Theta\Theta}$ and from Fig. 3 of Sec. III B that $C_{44} = C_{55} = C_{44}^0$, the condition on $g(R, \Theta)$ reduces to

$$g''_R + \frac{g'_R}{R} + \frac{g''_\Theta}{R^2} = 0. \quad (29)$$

To solve Eq. (29), we employ the method of separation of variables, and by taking into account the fourfold symmetry of the $\langle 001 \rangle$ copper wire, we assume the series solution for $g(R, \Theta)$ as

$$g(R, \Theta) = \sum_{N=1}^{+\infty} g_N R^{4N} \sin 4N\Theta, \quad (30)$$

where g_N are coefficients to be determined from the Gurtin and Murdoch surface conditions expressed in Eq. (17). Indeed, from the third relation in Eq. (17) combined with the expression of \mathbf{P} in Eq. (21) and \mathbf{P}^S in Eq. (23), we have

$$(S_{RZ} + F_{zR} S_{RR})|_{R=R_0} = \frac{1}{R_0} \frac{\partial}{\partial \Theta} (S_{\Theta Z}^S + F_{z\Theta}^S S_{\Theta\Theta}^S). \quad (31)$$

Then, using Eqs. (20) and (22), we obtain

$$\begin{aligned} & (R_0 C_{44}^0 - S_{\Theta\Theta}^S) g'_R(R_0, \Theta) \\ &= \frac{\partial}{\partial \Theta} \left(C_{44}^S + \frac{g'_\Theta(R_0, \Theta)}{R_0} (C_{44}^S + S_{\Theta\Theta}^S) \right) \end{aligned} \quad (32)$$

with

$$S_{\Theta\Theta}^S = S_{\Theta\Theta}^{S,0} + C_{22}^S u_0 + C_{23}^S w_0.$$

Finally for $\langle 001 \rangle$ copper nanowires, by considering the small values found for u_0 and w_0 in Fig. 2, it will be verified in Sec. IV once the surface parameters and $g(R, \Theta)$ have been calculated that even for radii R_0 as small as 2 or 3 nm in

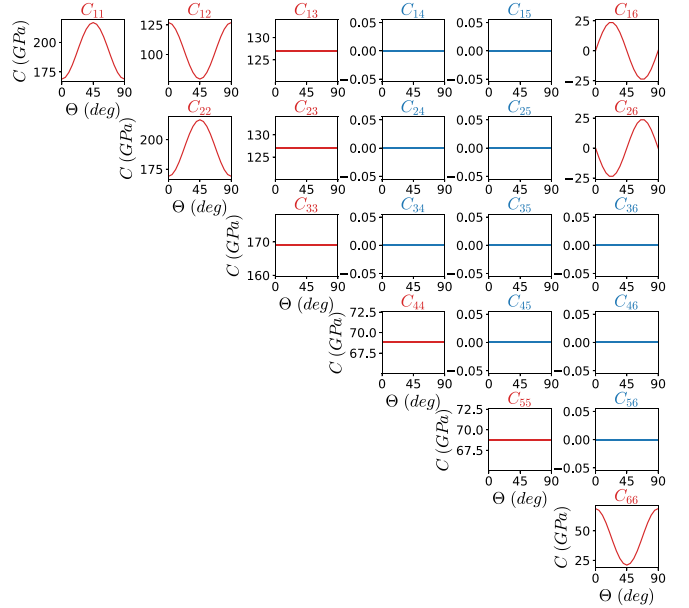


FIG. 3. Θ dependence of the second-order elastic constants C_{ij} in cylindrical coordinates according to Eqs. (42), the basis $(\mathbf{e}_R, \mathbf{e}_\Theta, \mathbf{e}_Z)$ is oriented such as \mathbf{e}_Z remains along a $\langle 001 \rangle$ direction. For $\Theta = 0$, \mathbf{e}_R and \mathbf{e}_Θ are also along $\langle 001 \rangle$ directions. See Sec. III A for more details.

Eq. (32), we have $R_0 C_{44}^0 \gg S_{\Theta\Theta}^S$ and $C_{44}^S \gg \frac{g'_\Theta(R_0, \Theta)}{R_0} (C_{44}^S + S_{\Theta\Theta}^S)$ leading to the simplified equation

$$g'_R(R_0, \Theta) = \frac{1}{R_0 C_{44}^0} \frac{\partial C_{44}^S}{\partial \Theta}. \quad (33)$$

This boundary condition on $g(R, \Theta)$ is a key relation in this work. In the isotropic case where C_{44}^S is constant, it is clear from Eq. (33) that C_{44}^S can not be responsible of a warp, $g'_R(R_0, \Theta)$ becomes null in Eq. (33), and the warping function $g(R, \Theta)$ in Eq. (30) must also vanish. Moreover, from Eq. (33), one can predict a warp if the surface elastic constant C_{44}^S varies with the azimuth Θ , i.e., if C_{44}^S depends on the surface orientation.

To test the validity of our model, molecular statics (MS) simulations are performed. The MS simulations are used both to calculate the pertinent physical parameters (notably, how varies C_{44}^S with Θ) in Sec. III and to determine the relaxed state of a $\langle 001 \rangle$ copper nanowire under torsion in Sec. IV.

III. ATOMISTIC CALCULATIONS

In this section, we first detail how the stress and strain tensors (\mathbf{F} , \mathbf{E} , \mathbf{S} , and \mathbf{P}) are determined knowing the atomic positions and using atomic interactions described within the SMA potential [13, 14]. Then, by performing molecular statics (MS) simulations on Cu slabs, we show how the surface elastic parameters ($S_{\Theta\Theta}^{S,0}$, $S_{ZZ}^{S,0}$, and C_{ij}^S) vary with the orientation of the surface slabs.

A. Atomic strain and stress tensors

Knowing both the position $\mathbf{X}^{(i)}$ of each atom i in the reference configuration and its position $\mathbf{x}^{(i)}$ in the deformed

and relaxed configuration, it is possible to calculate the local deformation gradient $\mathbf{F}^{(i)}$ at each atom i by considering how the distances with its neighbor atoms j have changed. Using a discrete form of Eq. (4), we have

$$\mathbf{x}^{(j)} - \mathbf{x}^{(i)} = \mathbf{F}^{(i)}(\mathbf{X}^{(j)} - \mathbf{X}^{(i)}). \quad (34)$$

In principle, three noncoplanar neighbors leads to a single $\mathbf{F}^{(i)}$, however, since the number of neighbors j is much larger, one has to search for an optimal local deformation gradient $\hat{\mathbf{F}}^{(i)}$ which minimizes a weighted least-squares error among the neighbors of i . For greater detail on this method which enables the calculation of the atomic tensor \mathbf{F} , the reader is referred to Gullett *et al.* [25]. In this work, we used a similar method which differs only by the choice of the number of neighbors j on the calculation of $\hat{\mathbf{F}}^{(i)}$. In our case, only the first-nearest neighbors j of the atom i are taken into account to compute $\hat{\mathbf{F}}^{(i)}$.

Once $\hat{\mathbf{F}}^{(i)}$ is calculated (denoted by $\mathbf{F}^{(i)}$ below for simplicity), the atomic strain tensor $\mathbf{E}^{(i)}$ is determined using the definition $\mathbf{E} = \frac{1}{2}(\mathbf{F}^T \mathbf{F} - \mathbf{I})$. Moreover, from the polar decomposition theorem, we have the unique multiplicative decomposition $\mathbf{F} = \mathbf{R}\mathbf{U}$ in which \mathbf{R} is called the rotation tensor (which is orthogonal, $\mathbf{R}^T \mathbf{R} = \mathbf{I}$) and \mathbf{U} is the right stretch tensor (which is symmetric and positive-definite, $\mathbf{U}^2 = \mathbf{F}^T \mathbf{F}$).

The analytic form of the SMA potential used in our atomistic simulations allows us a straightforward determination of the atomic strain energy $\psi^{(i)}$ per unit undeformed volume and therefore to the *second* Piola-Kirchhoff stress tensor (PK2) per atom i using the relation $\mathbf{S}^{(i)} = d\psi^{(i)}/d\mathbf{E}^{(i)}$. To calculate the six components $S_k^{(i)}$ of $\mathbf{S}^{(i)}$, let us first express the atomic strain energy $\psi^{(i)}$. According to the SMA potential, the energy W^i of the atom i having j neighbors can be written as the sum of a repulsive term $W_{\text{rep}}^{(i)}$ and an attractive term $W_{\text{att}}^{(i)}$:

$$W^{(i)} = W_{\text{rep}}^{(i)} + W_{\text{att}}^{(i)} = \sum_j \mathcal{W}_{\text{rep}}(r^{(ij)}) - \sqrt{\sum_j \mathcal{W}_{\text{att}}(r^{(ij)})}, \quad (35)$$

where \mathcal{W}_{rep} and \mathcal{W}_{att} are decreasing exponentials of the $r^{(ij)}$ distances between i and j atoms, i.e., the norms of the vectors $\mathbf{x}^{(j)} - \mathbf{x}^{(i)}$ in Eq. (34). In the reference state where atoms occupy the bulk crystal lattice, the norms of the vectors $\mathbf{X}^{(j)} - \mathbf{X}^{(i)}$ are denoted by $r_0^{(ij)}$ and far from the surface, the energy per atom is the cohesive energy $E_{\text{coh}} = \sum_j \mathcal{W}_{\text{rep}}(r_0^{(ij)}) - \sqrt{\sum_j \mathcal{W}_{\text{att}}(r_0^{(ij)})}$. Using these notations, the atomic strain energy density reads as

$$\psi^{(i)} = \frac{1}{V_0}(W^{(i)} - E_{\text{coh}}),$$

where V_0 is the atomic volume in the undeformed state. To summarize, from one atomic configuration, one gets per atom i , the energy $W^{(i)}$, the nine components $R_{nm}^{(i)}$ of the rotation tensor $\mathbf{R}^{(i)}$, and the six components $U_l^{(i)}$ of the right stretch tensor $\mathbf{U}^{(i)}$. By gathering these quantities, one obtains the PK2 stress tensor per atom $\mathbf{S}^{(i)}$ and its k components $S_k^{(i)}$ by calculating the following derivatives:

$$S_k^{(i)} = \frac{\partial \psi^{(i)}}{\partial E_k^{(i)}} = \frac{1}{V_0} \frac{\partial W^{(i)}}{\partial E_k^{(i)}} \quad (36)$$

or, equivalently,

$$S_k^{(i)} = \frac{1}{V_0} \sum_{l=1}^6 \frac{\partial W^{(i)}}{\partial U_l^{(i)}} H_{kl}^{(i)}, \quad (37)$$

where $H_{kl}^{(i)} = \frac{\partial U_l^{(i)}}{\partial E_k^{(i)}}$. In practice, to determine the 36 $H_{kl}^{(i)}$ elements of the matrix H it is easier to handle the invert matrix $G = H^{-1}$ whose elements $G_{kl}^{(i)} = \frac{\partial E_l^{(i)}}{\partial U_k^{(i)}}$ can be directly written from the relation $\mathbf{E} = \frac{1}{2}(\mathbf{U}^2 - \mathbf{I})$. Finally, in Eq. (37), the $\frac{\partial W^{(i)}}{\partial U_l^{(i)}}$ terms can be expressed as

$$\frac{\partial W^{(i)}}{\partial U_l^{(i)}} = \sum_j \left(\frac{\partial \mathcal{W}_{\text{rep}}(r^{(ij)})}{\partial r^{(ij)}} + \frac{1}{2\mathcal{W}_{\text{att}}^{(i)}} \frac{\partial \mathcal{W}_{\text{att}}(r^{(ij)})}{\partial r^{(ij)}} \right) \frac{\partial r^{(ij)}}{\partial U_l^{(i)}}, \quad (38)$$

where

$$\frac{\partial r^{(ij)}}{\partial U_l^{(i)}} = \frac{1}{2r^{(ij)}} \sum_{p=1}^3 r_p^{(ij)} (R_{pm}^i r_{0,n}^{(ij)} + R_{pn}^i r_{0,m}^{(ij)}) \quad (39)$$

with $r_p^{(ij)}$ and $r_{0,p}^{(ij)}$ denoting the Cartesian coordinates of, respectively, the vectors $\mathbf{x}^{(j)} - \mathbf{x}^{(i)}$ and $\mathbf{X}^{(j)} - \mathbf{X}^{(i)}$ such as $(r^{(ij)})^2 = (r_1^{(ij)})^2 + (r_2^{(ij)})^2 + (r_3^{(ij)})^2$ and $(r_0^{(ij)})^2 = (r_{0,1}^{(ij)})^2 + (r_{0,2}^{(ij)})^2 + (r_{0,3}^{(ij)})^2$. Note that each pair (m, n) of indices in Eq. (39) is determined by the single index l using the Voigt's convention. Thus, for $l = 1, 2$, or 3 where $U_l^{(i)}$ is diagonal we have $m = n = l$. For $l = 4$ then $m = 2$ and $n = 3$, for $l = 5$, $m = 1, n = 3$, and for $l = 6$, $m = 1, n = 2$.

To model the state of strain and stress in the nanowire, one needs to calculate the elastic constants given by the SMA potential. These latter are derived from the expansion of the bulk strain energy $\psi(\mathbf{E})$ per unit undeformed volume in a series of powers of \mathbf{E} such as

$$\psi(\mathbf{E}) = \frac{1}{2!} C_{ij}^0 E_i E_j + \frac{1}{3!} C_{ijk}^0 E_i E_j E_k + \dots, \quad (40)$$

where

$$C_{ij}^0 = \left. \frac{\partial^2 \psi(\mathbf{E})}{\partial E_i \partial E_j} \right|_{\mathbf{E}=\mathbf{0}}, \quad C_{ijk}^0 = \left. \frac{\partial^3 \psi(\mathbf{E})}{\partial E_i \partial E_j \partial E_k} \right|_{\mathbf{E}=\mathbf{0}}.$$

C_{ij}^0 and C_{ijk}^0 are called, respectively, second-order and third-order elastic (stiffness) constants and defined in the crystal axis coordinate system along the unit vectors $\mathbf{e}_1, \mathbf{e}_2, \mathbf{e}_3$. In practice, we determine numerically these elastic constants although analytic forms might be derived using the SMA potential. Using Eq. (37), we calculate the PK2 stress components S_i per atom in a simulation box where the atoms form a periodic fcc crystal submitted to a chosen set of simple deformations. These latter are tensile or compressive strains such as $\mathbf{E} = E_1 \mathbf{e}_1 \otimes \mathbf{e}_1$ or $\mathbf{E} = E_1 \mathbf{e}_1 \otimes \mathbf{e}_1 + E_2 \mathbf{e}_2 \otimes \mathbf{e}_2$, pure shear strain where for instance $\mathbf{E} = E_6/2(\mathbf{e}_1 \otimes \mathbf{e}_2 + \mathbf{e}_2 \otimes \mathbf{e}_1)$, or a combination of them where \mathbf{E} depends on two components only. For each of these deformations, it is straightforward to write the corresponding S_i 's components since from Eqs. (36) and (40) we have

$$S_i = C_{ij}^0 E_j + \frac{1}{2} C_{ijk}^0 E_j E_k + \dots \quad (41)$$

Then by combining Eq. (41) and polynomial fits of the S_i terms calculated from the simulations, we determine the

values of the 3 C_{ij}^0 and the 6 C_{ijk}^0 which are independent in the cubic system. In this work only linear terms involving C_{ij}^0 are used.

In order to relate the C_{ij}^0 determined in this section to the C_{ij} introduced in Eq. (19) and defined using cylindrical coordinates for $\langle 001 \rangle$ fcc copper wires, it is necessary to apply the rules governing the change of the elastic constants under such a transformation of coordinates [18]. Thus, after transformation, 11 C_{ij} are not null and depend with the azimuth Θ as follows:

$$\begin{aligned} C_{11} &= C_{22} = C_{11}^0 + C_c^0 (\cos 4\Theta - 1), \\ C_{12} &= C_{12}^0 - C_c^0 (\cos 4\Theta - 1), \\ C_{13} &= C_{23} = C_{12}^0, \\ C_{16} &= -C_{26} = -C_c^0 \sin 4\Theta, \\ C_{33} &= C_{11}^0, \\ C_{44} &= C_{55} = C_{44}^0, \\ C_{66} &= C_{44}^0 - C_c^0 (\cos 4\Theta - 1), \end{aligned} \quad (42)$$

where $C_c^0 = (C_{11}^0 - C_{12}^0 - 2C_{44}^0)/4$. These relations remind us that despite its high fourfold symmetry the $\langle 001 \rangle$ directions in cubic system present an anisotropy of the in-plane elastic constant (i.e., C_{11} and C_{12} vary with Θ) which has to be taken into account to solve the mechanical problem addressed in this work. To illustrate this important property, Fig. 3 shows the dependencies of C_{ij} with the azimuth Θ to be considered in Eqs. (19) and (20).

B. Surface excess elastic parameters

By performing molecular statics (MS) simulations on various Cu slabs, the dependencies with the azimuth Θ of the surface elastic parameters $S_{\Theta\Theta}^{S,0}$, $S_{ZZ}^{S,0}$, and C_{ij}^S which appear in Eqs. (22) are calculated. This step is essential to estimate how the PK2 surface stress tensor \mathbf{S}^S at the surface of the wire varies with the surface strain \mathbf{E}^S in the framework of the linear elasticity theory established in Sec. II A. To quantify the parameters $S_{\Theta\Theta}^{S,0}$, $S_{ZZ}^{S,0}$, and C_{ij}^S for a certain azimuth Θ at the surface of the wire, we first note that for a given value of Θ , the surface of the wire of circular cross section resembles locally to an unreconstructed vicinal surface (with atomic straight steps and terraces) which is reproduced from a slab where \mathbf{e}_R indicates the orientation of vicinal surface and where its atomic steps are along \mathbf{e}_Z and normal to \mathbf{e}_Θ . In-plane periodic boundary conditions are applied to this slab presenting an integer number of terraces and, as previously for the determination of the bulk elastic constants, a set of simple strains \mathbf{E} expressed now in terms of the unit vectors \mathbf{e}_R , \mathbf{e}_Θ , and \mathbf{e}_Z is imposed to the slab. Using Eq. (36), the PK2 stress per atom $\mathbf{S}^{(i)}$ is calculated for each atom (i) in the deformed slab after relaxation of its two surfaces by MS simulations.

Following the method described by Needs [26], the surface stress \mathbf{S}^S is defined as an excess quantity (in J m^{-2}) where the contribution of each atom (i) in the slab to \mathbf{S}^S is obtained by subtracting from the stress $\mathbf{S}_{\text{slab}}^{(i)}$ of each atom (i) in the slab the stress $\mathbf{S}_{\text{bulk}}^{(i)}$ that this atom would have if it was subjected to

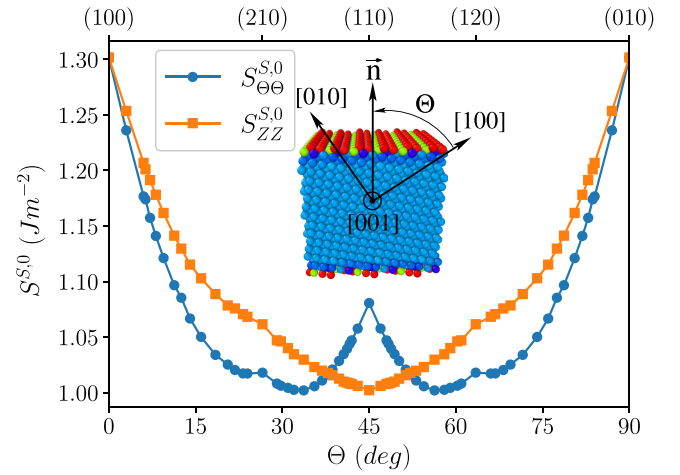


FIG. 4. Plot of the surface parameters $S_{\Theta\Theta}^{S,0}$ and $S_{ZZ}^{S,0}$ introduced in Eqs. (22) as a function of Θ calculated from MS simulations using the SMA potential on various Cu slabs presenting different vicinal surfaces (hk0) sharing the same [001] direction corresponding to the $\langle 001 \rangle$ nanowire axis. As an example, the case of a slab with (230) surfaces corresponding to a value of $\Theta \approx 56.31^\circ$ is shown.

the same strain \mathbf{E} in the bulk. Mathematically, we have

$$\mathbf{S}^S(\mathbf{E}^S) = \frac{V_0}{2A_0} \sum_{i \in \text{slab}} [\mathbf{S}_{\text{slab}}^{(i)}(\mathbf{E}) - \mathbf{S}_{\text{bulk}}^{(i)}(\mathbf{E})], \quad (43)$$

where the factor $\frac{1}{2}$ comes from the two surfaces of the slab of area A_0 before deformation and $\mathbf{E}^S = \mathbf{I}^S \mathbf{E} \mathbf{I}^S$ as defined in Sec. II A. In practice, thick slabs are considered and $\mathbf{S}_{\text{bulk}}^{(i)}$ is calculated from atoms (i) chosen at the center of the slab far from the surfaces.

Considering first the simple case where $\mathbf{E} = \mathbf{E}^S = \mathbf{0}$ and many different vicinal surfaces presenting straight steps along the $\langle 001 \rangle$ direction, we report in Fig. 4 the Θ dependencies of the components $S_{\Theta\Theta}^{S,0}$ and $S_{ZZ}^{S,0}$ introduced in Eqs. (22) and calculated from Eq. (43). According to our MS simulations using the SMA potential, $S_{\Theta\Theta}^{S,0}$ and $S_{ZZ}^{S,0}$ present similar behaviors with a maximum value (around 1.3 J m^{-2}) for the highly symmetric $\{100\}$ surface where $\Theta = 0$. For surfaces with lesser symmetry, $S_{\Theta\Theta}^{S,0}$ decreases faster than $S_{ZZ}^{S,0}$, however, the two curves cross by approaching the $\{110\}$ surface. For this latter orientation encountered for $\Theta = \pi/4$, $S_{ZZ}^{S,0}$ (close to 1 J m^{-2}) becomes slightly lower than $S_{\Theta\Theta}^{S,0}$ but the difference does not exceed 10%. To determine the surface elastic constants C_{ij}^S in Eqs. (22), the slabs are now homogeneously strained according to simple deformations where $\mathbf{E}^S = \mathbf{E}$ such as $\mathbf{E} = E_{\Theta\Theta}^S \mathbf{e}_\Theta \otimes \mathbf{e}_\Theta + E_{ZZ}^S \mathbf{e}_Z \otimes \mathbf{e}_Z$ and $\mathbf{E} = E_{\Theta Z}^S (\mathbf{e}_\Theta \otimes \mathbf{e}_Z + \mathbf{e}_Z \otimes \mathbf{e}_\Theta)$. Then, by calculating numerically the strain derivatives of the $\mathbf{S}^S(\mathbf{E}^S)$ components obtained from Eq. (43), we plot in Fig. 5 the Θ dependencies of the surface elastic constants C_{ij}^S . We observe that the C_{ij}^S have maximum values for the $\{100\}$ surface where $\Theta = 0$ while they are close to their lowest values for the $\{110\}$ surface where $\Theta = \pi/4$.

These calculations clearly show the anisotropy of the surface elastic constants which is present at the lateral surface of the $\langle 001 \rangle$ copper wires of circular cross section. In particular, it is demonstrated that the constant C_{44}^S varies significantly

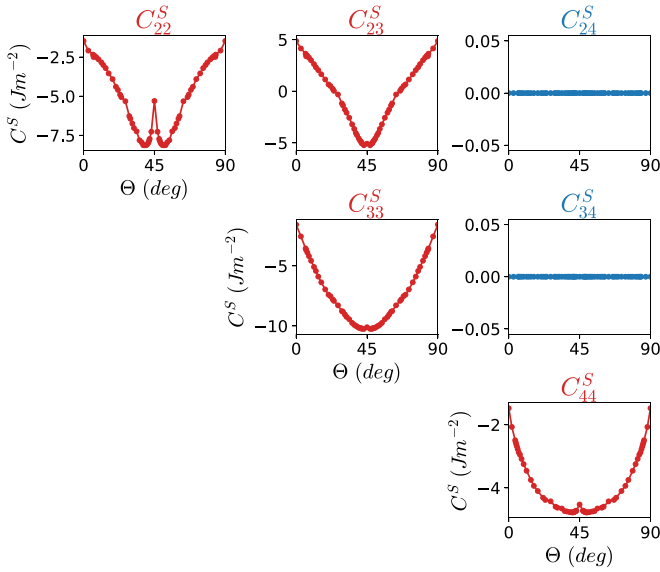


FIG. 5. Θ dependencies of the surface elastic constants C_{ij}^S calculated from MS simulations on strained slabs presenting vicinal surfaces. The orientation of the unit vectors \mathbf{e}_R , \mathbf{e}_Θ , and \mathbf{e}_z is such that \mathbf{e}_R is normal to the surface and \mathbf{e}_z is along the $\langle 001 \rangle$ atomic steps. The index convention to identify the C_i^S is the one given in Eqs. (19) and (22) where the index “2” denotes “ $\Theta\Theta$,” “3” stands for “ZZ,” and “4” corresponds to “ ΘZ .”

with Θ . According to the continuum model developed in Sec. II, such an anisotropic behavior of C_{44}^S should give rise to a warp in the wire under torsion. To test this theoretical prediction, atomistic simulations are performed in the next section.

IV. EVIDENCE OF A WARP CAUSED BY SURFACE ELASTICITY: FROM ATOMISTIC SIMULATIONS TO CONTINUUM MODEL

The last part of this work is to examine the ability of our continuum model to reproduce the results of atomistic simulations, in particular the C_{44}^S -induced warping. For this purpose, using torsion periodic boundary conditions, molecular statics (MS) calculations are performed to simulate an infinite twisted $\langle 001 \rangle$ copper nanowire [24]. According to the expression of the deformation gradient tensor \mathbf{F} envisaged in this work in Eq. (5), the signature of the warp will appear in the two components $F_{zR} = \alpha R_0 g'_R$ and $F_{z\Theta} = \alpha R_0 g'_\Theta / R$ that both depend on the warping function $g(R, \Theta)$ expressed in Eq. (30). Using the method described in Sec. III A to calculate the local deformation gradient $\mathbf{F}^{(i)}$ at each atom i , we report in Fig. 6 the (R, Θ) dependencies of F_{zR} and $F_{z\Theta}$ observed in a cross section of a simulated $\langle 001 \rangle$ copper wire of radius $R_0 = 30$ nm twisted to $\alpha = -2.56 \times 10^{-4}$ rad/nm. Clearly, Fig. 6 shows the presence of a warp compatible with the fourfold symmetry of the function $g(R, \Theta)$ predicted in Eq. (30) of our model. Let us now examine if it is possible to rationalize the warp observed in our atomistic simulations by reproducing F_{zR} and $F_{z\Theta}$ from the continuum model developed in this work. For this purpose, we need to determine the coefficients g_N defining $g(R, \Theta)$ in Eq. (30) from the boundary condition established

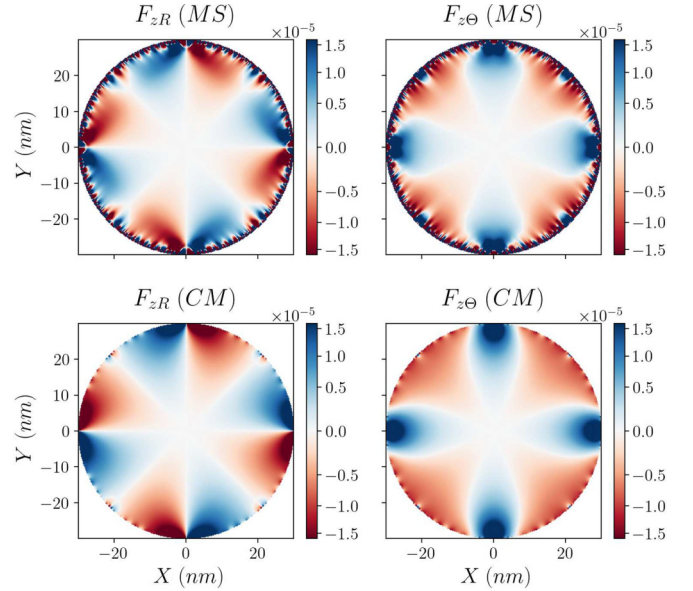


FIG. 6. F_{zR} and $F_{z\Theta}$ in a cross section of a $\langle 001 \rangle$ copper wire of radius $R_0 = 30$ nm twisted to $\alpha = -2.56 \times 10^{-4}$ rad/nm. Maps are obtained from both our molecular statics simulations (MS) and our continuum model (CM).

in Eq. (33) which states that $g'_R(R_0, \Theta)$ is proportional to $\partial C_{44}^S / \partial \Theta$. This can be achieved from an expansion in Fourier series of C_{44}^S obtained in Fig. 5. To illustrate the harmonic analysis, Fig. 7 shows the behavior of $\partial C_{44}^S / \partial \Theta$ as a function of Θ deduced from our atomistic calculations performed on different slabs. After an interpolation (using cubic splines) between the points where C_{44}^S were computed, we calculate the Fourier coefficients of C_{44}^S which are sufficient to well describe

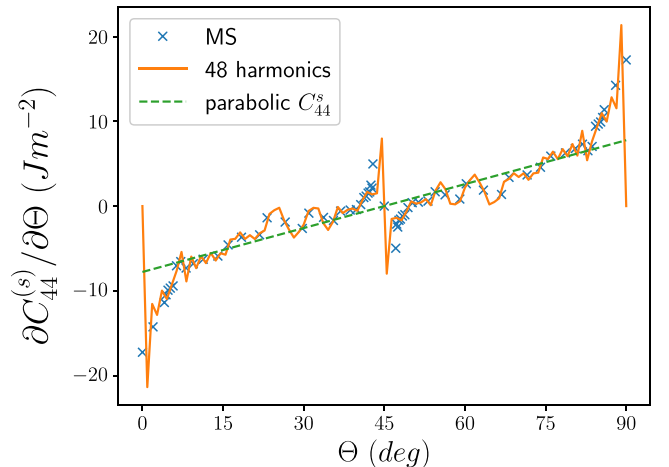


FIG. 7. Modeling of the surface elastic constant $C_{44}^S(\Theta)$ calculated from the MS simulations and shown in Fig. 5. In this figure, its derivative $\partial C_{44}^S / \partial \Theta$ that appears in the boundary condition given by Eq. (33) is first reproduced from a Fourier series expansion by retaining the first 48 harmonics (orange solid line). These Fourier coefficients set the values of the coefficients c_N in Eq. (44). The green dashed line is plotted from Eq. (49) where $\partial C_{44}^S / \partial \Theta$ is approximated by a sawtooth function [and $C_{44}^S(\Theta)$ by a parabola in Eq. (48)].

C_{44}^S and $\frac{\partial C_{44}^S}{\partial \Theta}$ (by derivation with respect to Θ) as shown in Fig. 7. The Fourier analysis shows that in our case, only the terms in $\sin 4N\Theta$ are necessary to represent $\frac{\partial C_{44}^S}{\partial \Theta}$ so that

$$\frac{\partial C_{44}^S}{\partial \Theta} = \sum_{N=1}^{+\infty} c_N \sin 4N\Theta, \quad (44)$$

where c_N are the Fourier coefficients. Once the c_N are computed, it is straightforward to determine the g_N . By combining Eqs. (30) and (33), we find

$$g_N = \frac{c_N}{4NC_{44}^0 R_0^{4N}} \quad (45)$$

and therefore

$$F_{zR} = \alpha R_0 g'_R = \frac{\alpha}{C_{44}^0} \sum_{N=1}^{+\infty} c_N \left(\frac{R}{R_0}\right)^{4N-1} \sin 4N\Theta, \quad (46)$$

$$F_{z\Theta} = \alpha R_0 g'_\Theta / R = \frac{\alpha}{C_{44}^0} \sum_{N=1}^{+\infty} c_N \left(\frac{R}{R_0}\right)^{4N-1} \cos 4N\Theta. \quad (47)$$

The c_N being deduced from the Fourier analysis of C_{44}^S , it becomes possible to test the continuum model by plotting F_{zR} and $F_{z\Theta}$ from Eqs. (46) and (47). The comparison with the results of our atomistic simulations is reported in Fig. 6 and shows a very good quantitative agreement between the two approaches.

This understanding of the results of our atomistic simulations allows us to pursue the description of the observed warp to other elements than copper by proposing a simplified model that can be extended to any wire with a cubic, $\langle 001 \rangle$ -oriented crystalline structure and a circular cross section [as long as the simplification of Eq. (32) which leads to Eq. (33) and gives a preponderant role to C_{44}^S , remains valid for an element other than copper]. Indeed, this study shows that as soon as the elastic shear constant C_{44}^S depends on the orientation of the surface and thus varies with the azimuth Θ , we can expect to observe a warp whose shape is deduced directly from Eqs. (46) and (47).

If in addition C_{44}^S varies smoothly and adopts a parabolic shape with Θ on the interval $[0 : \pi/2]$ as can be observed for copper in Fig. 5, it is possible to derive an analytic form of the warp function. Let us suppose that the parabolic form of C_{44}^S is fixed by its extreme values obtained for the two surfaces $\{100\}$ and $\{110\}$, i.e., by $[C_{44}^S(0)$ and $C_{44}^S(\pi/4)]$, such that

$$C_{44}^S = C_{44}^S(\pi/4) + (4/\pi)^2 [C_{44}^S(0) - C_{44}^S(\pi/4)] (\Theta - \pi/4)^2, \quad (48)$$

thus,

$$\frac{\partial C_{44}^S}{\partial \Theta} = 2(4/\pi)^2 [C_{44}^S(0) - C_{44}^S(\pi/4)] (\Theta - \pi/4). \quad (49)$$

$\frac{\partial C_{44}^S}{\partial \Theta}$ can thus be modeled by a sawtooth function of slope equal to $a = 2(4/\pi)^2 [C_{44}^S(0) - C_{44}^S(\pi/4)]$ as plotted in Fig. 7 for $\Theta \in [0 : \pi/2]$. For any Θ , $\frac{\partial C_{44}^S}{\partial \Theta}$ is described by the series

$$\frac{\partial C_{44}^S}{\partial \Theta} = -\frac{a}{2} \sum_{N=1}^{+\infty} \frac{\sin 4N\Theta}{N} \quad (50)$$

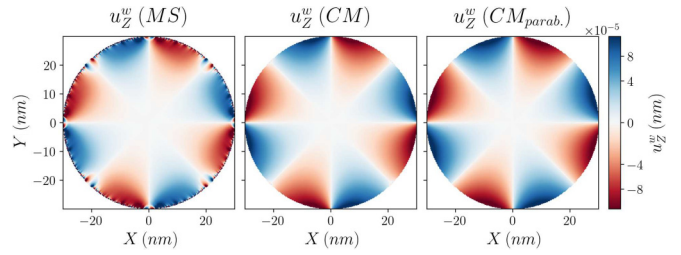


FIG. 8. Comparison of the warp u_z^w (MS) observed in the atomistic simulations with u_z^w (CM) predicted by the continuum model in Eq. (54) where the c_N are determined from the Fourier analysis of C_{44}^S shown in Fig. 7. The displacement field u_z^w (CM_{parab.}) assuming a parabolic form of C_{44}^S in Eq. (55) is also plotted. $R_0 = 30$ nm and $\alpha = -2.56 \times 10^{-4}$ rad/nm.

which sets the c_N at

$$c_N = -\frac{a}{2N} = -\frac{(4/\pi)^2 [C_{44}^S(0) - C_{44}^S(\pi/4)]}{N} \quad (51)$$

and leads to the following expressions of F_{zR} and $F_{z\Theta}$:

$$F_{zR} = \alpha R_0 g'_R = \frac{-\alpha a}{2C_{44}^0} \sum_{N=1}^{+\infty} \left(\frac{R}{R_0}\right)^{4N-1} \frac{\sin 4N\Theta}{N}, \quad (52)$$

$$F_{z\Theta} = \alpha R_0 g'_\Theta / R = \frac{-\alpha a}{2C_{44}^0} \sum_{N=1}^{+\infty} \left(\frac{R}{R_0}\right)^{4N-1} \frac{\cos 4N\Theta}{N}. \quad (53)$$

Finally, it can be interesting to establish the expression of the warp u_z^w itself which represents the displacement field of the atoms along the wire axis induced by the torsion. Since from Eq. (2), $u_z^w = \alpha R_0 g(R, \Theta)$, we obtain from Eqs. (30) and (45) the general form

$$u_z^w = \alpha \sum_{N=1}^{+\infty} \frac{c_N R_0}{4N C_{44}^0} \left(\frac{R}{R_0}\right)^{4N} \sin 4N\Theta \quad (54)$$

which, by considering Eq. (51), leads to the particular form

$$u_z^w = \frac{-4\alpha R_0 [C_{44}^S(0) - C_{44}^S(\pi/4)]}{\pi^2 C_{44}^0} \sum_{N=1}^{+\infty} \left(\frac{R}{R_0}\right)^{4N} \frac{\sin 4N\Theta}{N^2} \quad (55)$$

when C_{44}^S is parabolic. The displacement fields u_z^w (CM) given by Eq. (54), u_z^w (CM_{parab.}) from Eq. (55), and u_z^w (MS) from the atomistic simulations are compared in Fig. 8 for $R_0 = 30$ nm and a torsion $\alpha = -2.56 \times 10^{-4}$ rad/nm. Clearly, the three approaches give similar results on the overall shape of u_z^w . For copper, even u_z^w (CM_{parab.}) that relies on the modeling of $\frac{\partial C_{44}^S}{\partial \Theta}$ by a sawtooth function is quite relevant to capture the main characteristics of the warp. Of course, the atomistic description reveals details about u_z^w at the vicinity of the surface that are not predicted with the continuum model. We can see for instance in Fig. 8 that lobes appear under the step edges of the $\{100\}$ and the $\{110\}$ surfaces. Apart from these differences related to the surface morphology at the atomic scale, both the MS simulations and the continuum model predict a very similar warp induced by the torsion. These results lead us to additional comments.

First, it is interesting to note that Eq. (55) indicates what are the physical ingredients which control the amplitude of the warp in copper: namely, the ratio $[C_{44}^S(0) - C_{44}^S(\pi/4)]/C_{44}^0$ where $C_{44}^S(0)$ and $C_{44}^S(\pi/4)$ are the surface shear elastic constants of, respectively, the $\{100\}$ and the $\{110\}$ surfaces and where C_{44}^0 is the bulk shear elastic constant. Let us keep in mind that this result was obtained in the framework of the SMA potential where C_{44}^S could be approximated by a parabola with $C_{44}^S(0)$ and $C_{44}^S(\pi/4)$ as extreme values. It would be interesting to see if such a behavior is found in other elements.

Second, it is worth pointing out that the warp appears as soon as α is nonzero. It is induced by the torsion. This phenomenon is different from the case studied by Roy *et al.* [27] where in absence of torsion it is shown a wrinkling of the $\langle 111 \rangle$ atomic planes normal to the wire axis for single-crystalline $\langle 111 \rangle$ Au nanowire of hexagonal cross section. By performing MS simulations with the SMA potential on $\langle 111 \rangle$ Cu wire with circular cross section, we also observe such a wrinkling of the $\langle 111 \rangle$ atomic planes for $\alpha = 0$. However, in this work where we focus on $\langle 001 \rangle$ -oriented wires the wrinkling does not occur.

A third point is how large this effect is. As it is the sole nonuniform u_z displacement here, a comparison has to be done with the warp in another situation, namely, the dominant warp related to bulk elastic anisotropy, generated by torsion in Cu $\langle 011 \rangle$ nanowires. This latter warp is a good reference since it was shown to be measurable using x-ray diffraction [15], which is a selective and sensitive technique. The ratio between the Cu $\langle 011 \rangle$ and $\langle 001 \rangle$ warps, for the same torsion α and nanowire radius R_0 , is proportional to R_0 and equal to approximately 90 when $R_0 = 6$ nm. We believe therefore that, at least in the case of Cu, the $\langle 001 \rangle$ torsion warp would be difficult to measure using x-ray diffraction, even using high-order reflections.

Finally, it is important to recall that the domain of validity of our model concerns moderate torsion where the warp remains proportional to α . If the analysis of the nonlinear domain in α is beyond the scope of this study, it is however instructive to take a look at the behavior of u_z^w for larger torsions according to the simulations. This is illustrated in Fig. 9 where we show examples of u_z^w atomic fields obtained in the MS simulations for different α and a wire of radius $R_0 = 6$ nm. In order to show the linear regime, we also report as a function of α , the magnitude of $u_z^w/u_z^w(\alpha_0)$ at different arbitrarily chosen points of the wire section and for α_0 chosen in the linear regime. The linear domain is clearly visible on Fig. 9. It is observed within the interval $|\alpha|R_0 < 0.02$ for $R_0 = 6$ nm. Beyond this threshold value, $u_z^w/u_z^w(\alpha_0)$ is no longer proportional to α . Its dependence varies with (R, Θ) . The figure also shows some snapshots extracted from the simulations for different values of α . The atoms are colored with the same color scale according to the value of their displacement normalized by $|\alpha|$. The first two snapshots in the linear regime highlight the existence of the warp in agreement with our model and Fig. 8. Normalized by $|\alpha|$, the two snapshots are logically nearly identical. Beyond the linear regime, we can note from the snapshots that the warp seems to exhibit additional harmonics weighted by higher R powers, so that the warp seems to be more concentrated on the wire periphery.

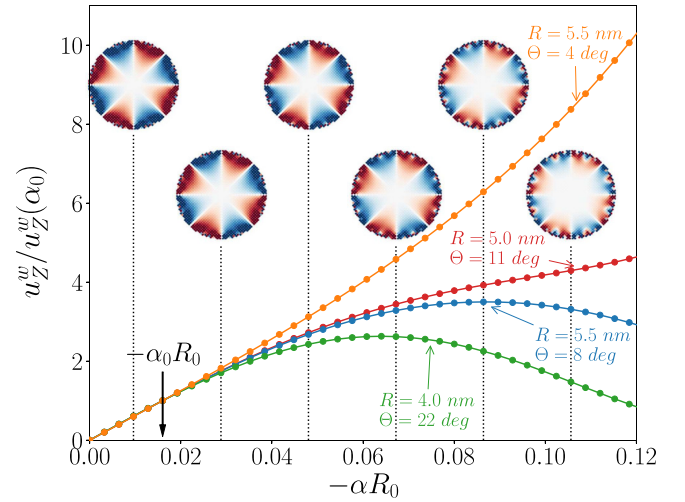


FIG. 9. Examples of u_z^w atomic displacement fields obtained from MS simulations for different α and a wire of radius $R_0 = 6$ nm. To show the linear regime, the ratios $u_z^w/u_z^w(\alpha_0)$ for arbitrarily chosen points of the wire section are plotted as a function of $-\alpha R_0$ and for α_0 chosen in the linear regime. Snapshots taken for different values of α are also shown. The atoms are colored with the same color scale according to the value of their displacement u_z^w normalized by $|\alpha|$.

Detailed analysis of this nonlinear domain remains to be done in the future, and it is interesting to note that nanowires are prime objects to explore the nonlinear elastic regime. Unlike in macroscopic wires, dislocations in nanowires appear indeed for high- α values only.

V. CONCLUSION

In linear elasticity, the moderate torsion of a $\langle 001 \rangle$ single-crystal copper wire with a circular cross section should not lead any displacement field along the wire axis (i.e., a warp). This result, well known in mechanics since the work of Saint Venant [9], is not observed in our atomistic simulations where we show on the contrary that a fourfold-symmetric warp appears as soon as there is a torsion. This intriguing finding is obtained by performing molecular statics simulations using the SMA interatomic potential for copper on $\langle 001 \rangle$ -oriented single-crystal nanowires with circular cross section and radii ranging from 3 to 30 nm. To elucidate the warp observed in our simulations we derive a continuum model based on the following assumptions.

We adopt a semi-inverse approach by assuming in Eq. (2) that the twist α has the effect of displacing the atoms along the Z axis of the wire according to a trial function $\alpha R_0 g(R, \Theta)$. Assuming such a warp, we establish the form taken by $g(R, \Theta)$ to satisfy the equilibrium equations and the boundary conditions.

The deformations are described in the framework of the finite strain theory. Indeed, although the deformations are small in this study, it is necessary to handle the finite strain tensor \mathbf{E} expressed in Eq. (7) to deal with the large rotations encountered in the torsion problem.

Since the strain is small, linear elasticity is used to express the second Piola-Kirchhoff stress tensor \mathbf{S} as a function of the finite strain tensor \mathbf{E} . The second-order elastic constants

C_{ij} involved in these relations are calculated using the SMA potential.

The Gurtin and Murdoch theory is employed to describe the surface-specific elastic properties. These are captured by the relationship between the surface stress tensor \mathbf{S}^S and the surface strain \mathbf{E}^S via surface elastic constants C_{ij}^S . In addition, this theory provides the boundary conditions (also called Young-Laplace conditions) of our problem linking the surface components of \mathbf{S}^S to certain bulk components of \mathbf{S} .

To keep a general formulation in cylindrical coordinates of our problem, the *first* Piola-Kirchhoff stress tensor \mathbf{P} is used to express the bulk equilibrium conditions in Eq. (12) and the boundary conditions in Eqs. (15) and (18). This formalism could be useful in the future to allow an exploration of the nonlinear domain.

To compare continuum model and atomistic simulations, care was taken to calculate stress and strain tensors at the atomic scale. In Sec. III, we describe in particular the method which allows us to determine a local deformation gradient tensor $\mathbf{F}^{(i)}$ at each atom i and the *second* Piola-Kirchhoff stress tensor $\mathbf{S}^{(i)}$ per atom i using the SMA potential. Moreover, for the comparison to be quantitative, all the physical ingredients involved in the model are calculated using the SMA potential. The dependence in Θ of the surface elastic constants C_{ij}^S which is a key point of this work has required additional calculations on deformed slabs presenting vicinal surfaces.

Within this theoretical framework, it is possible to understand the presence of a warp evidenced in this work for copper wires. The effect of the torsion is primarily to shear the atomic planes perpendicular to the wire axis. This shear strain is maximum at the surface and involves the surface elastic constant C_{44}^S in the expression of the component $P_{z\Theta}^S$ of the PK1 surface stress \mathbf{P}^S . The key point is then to realize that C_{44}^S like all surface elastic constants vary according to the local orientation of the lateral surface. This anisotropy of C_{44}^S could be quantified in our atomistic calculations using the SMA potential. This dependence with Θ of C_{44}^S has the effect of modifying [via the third Young-Laplace equation (17)] the boundary condition of the bulk stress component P_{zR} . In other words, $P_{zR}|_{R=R_0}$ is no longer null as it is the case when C_{44}^S is isotropic. This modification of the surface conditions gives rise to a nonzero P_{zR} component in the core of the wire which is solution of the third equilibrium equation expressed in Eqs. (14). The resolution of the differential equation (14) within the above-mentioned boundary condition allows us to derive an explicit form of the displacement field $u_z^w = \alpha R_0 g(R, \Theta)$ (i.e., the warp) envisaged in the deformation map given by Eq. (2). In Eq. (54), the expression of u_z^w is established as a function of the Fourier coefficients describing the variations of C_{44}^S with Θ . With the SMA potential set for copper, we observe a parabolic dependence of $C_{44}^S(\Theta)$, which allows us to propose an analytic form of the warp u_z^w whose amplitude is proportional to the ratio $\alpha R_0 \frac{[C_{44}^S(0) - C_{44}^S(\frac{\pi}{4})]}{C_{44}^0}$ where R_0 is the radius wire, C_{44}^0 the elastic shear constant in volume, $C_{44}^S(0)$ the elastic constant of the $\{100\}$ surface, and $C_{44}^S(\frac{\pi}{4})$ the one of the $\{110\}$ surface. The results obtained in this work could be extended to other

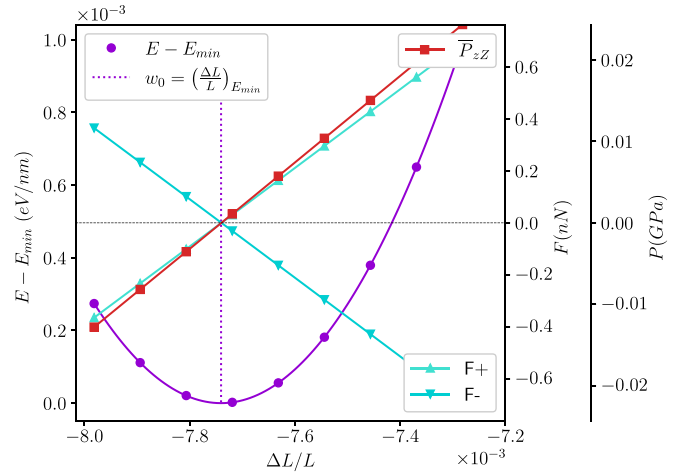


FIG. 10. Illustration from our atomistic simulations of the integral equilibrium condition given in Eq. (18) on a cross section S of a circular untwisted nanowire of radius $R_0 = 3$ nm subject to a change of length $\Delta L/L$. At equilibrium, the energy E of the wire (per unit length) is minimum for $\Delta L/L = w_0$, the net forces F^+ and F^- normal to S exerted by one part of the wire on the other are null, the sum $\bar{P}_{zZ} = \sum_{i \in S} P_{zZ}^{(i)}$ for all atoms i belonging to the cross section S is also null in agreement with Eq. (18).

monocrystalline wires of cubic structure, oriented $\langle 001 \rangle$ and of circular section. More fundamentally, this study tells us that in the torsion problem of a nanowire, the elastic properties of the lateral surface contribute to the formation of a warp in the bulk and may even be its sole cause as it is shown in this work for $\langle 001 \rangle$ circular cross-section Cu nanowires.

APPENDIX: INTEGRAL EQUILIBRIUM CONDITION

In addition to the Young-Laplace boundary conditions expressed in Eq. (17), one has to take in account the integral equilibrium condition in Eq. (18) valid for long wire free to relax along its main axis (no end effects). This condition is illustrated in this Appendix and verified even for very thin nanowire. Atomistic calculations for an untwisted nanowire of radius $R_0 = 3$ nm are reported in Fig. 10. First, we calculate from our MS simulations the total energy E of the nanowire as a function of its length l (the initial length being L). A minimum is reached for $E = E_{min}$ and $(l - L)/L = \Delta L/L = w_0$ as described in Sec. II B. Then, considering two parts of the wire separated by the cross section S , we plot in Fig. 10 the net forces F^+ and F^- normal to S exerted by one part on the other. We then note that the net forces F^+ and F^- are opposite for any l and null at equilibrium. This equilibrium state can be formulated in Eq. (18) in terms of the PK1 stress tensors \mathbf{P} and \mathbf{P}^S . To test Eq. (18) in our simulations, we plot in Fig. 10 the sum $\bar{P}_{zZ} = \sum_{i \in S} P_{zZ}^{(i)}$ for all atoms i belonging to a same cross section S and where the components $P_{zZ}^{(i)}$ are calculated from the atomic tensors $\mathbf{F}^{(i)}$ and $\mathbf{S}^{(i)}$ and the relation $\mathbf{P}^{(i)} = \mathbf{F}^{(i)}\mathbf{S}^{(i)}$. As expected from Eq. (18), we find that \bar{P}_{zZ} is null at equilibrium.

- [1] A. Sofiah, M. Samykano, K. Kadirgama, R. Mohan, and N. Lah, *Appl. Mater. Today* **11**, 320 (2018).
- [2] M. Nasr Esfahani and B. E. Alaca, *Adv. Eng. Mater.* **21**, 1900192 (2019).
- [3] H. Liang, M. Upmanyu, and H. Huang, *Phys. Rev. B* **71**, 241403(R) (2005).
- [4] C. R. Weinberger and W. Cai, *J. Mater. Chem.* **22**, 3277 (2012).
- [5] C. R. Weinberger and W. Cai, *Nano Lett.* **10**, 139 (2010).
- [6] J. D. Eshelby, *J. Appl. Phys.* **24**, 176 (1953).
- [7] J.-M. Roussel and M. Gailhanou, *Phys. Rev. Lett.* **115**, 075503 (2015).
- [8] B. Elsner, S. Müller, S. Bargmann, and J. Weissmüller, *Acta Mater.* **124**, 468 (2017).
- [9] S. Timoshenko and J. Goodier, *Theory of Elasticity*, 2nd ed. (McGraw-Hill, New York, 1951).
- [10] T. Chen, M.-S. Chiu, and C.-N. Weng, *J. Appl. Phys.* **100**, 074308 (2006).
- [11] M. Gurtin and A. Murdoch, *Arch. Ration. Mech. Anal.* **57**, 291 (1975).
- [12] J. Bonet and R. D. Wood, *Nonlinear Continuum Mechanics for Finite Element Analysis*, 2nd ed. (Cambridge University Press, Cambridge, 2008).
- [13] J. Creuze, F. Berthier, R. Tétot, and B. Legrand, *Phys. Rev. B* **62**, 2813 (2000).
- [14] J.-M. Roussel, S. Labat, and O. Thomas, *Phys. Rev. B* **79**, 014111 (2009).
- [15] M. Gailhanou and J.-M. Roussel, *J. Appl. Cryst.* **51**, 1586 (2018).
- [16] F. Murnaghan, *Finite Deformation of an Elastic Solid*, Applied Mathematics Series (Wiley, New York, 1951).
- [17] G. Wang, Z. He, and Q. Chen, *Appl. Math. Modell.* **96**, 697 (2021).
- [18] C. Teodosiu, *Elastic Models of Crystal Defects* (Springer, Berlin, 1982).
- [19] A. Javili and P. Steinmann, *Int. J. Solids Struct.* **47**, 3245 (2010).
- [20] K. Y. Volokh, *Mechanics of Soft Materials* (Springer, Berlin, 2016).
- [21] A. Javili, N. S. Ottosen, M. Ristinmaa, and J. Mosler, *Math. Mech. Solids* **23**, 1004 (2018).
- [22] P. Steinmann and O. Häsner, *Arch. Appl. Mech.* **75**, 31 (2005).
- [23] K. Brugger, *Phys. Rev.* **133**, A1611 (1964).
- [24] M. Gailhanou and J.-M. Roussel, *Phys. Rev. B* **88**, 224101 (2013).
- [25] P. M. Gullett, M. F. Horstemeyer, M. I. Baskes, and H. Fang, *Modell. Simul. Mater. Sci. Eng.* **16**, 015001 (2008).
- [26] R. J. Needs, *Phys. Rev. Lett.* **58**, 53 (1987).
- [27] A. Roy, S. Kundu, K. Müller, A. Rosenauer, S. Singh, P. Pant, M. P. Gururajan, P. Kumar, J. Weissmüller, A. K. Singh *et al.*, *Nano Lett.* **14**, 4859 (2014).